

# Experimental and numerical investigation on the stability of a high arch dam with typical problems of nonsymmetry: Baihetan Dam, China

Ziheng Song<sup>1</sup> · Yaoru Liu<sup>1</sup> · Qiang Yang<sup>1</sup>

Received: 1 July 2015 / Accepted: 11 November 2015 / Published online: 24 November 2015  
© Springer-Verlag Berlin Heidelberg 2015

**Abstract** High arch dams present nonsymmetry problems, both on topological and geological conditions at dam site, and are inevitable in many projects. Their influence is unfavorable to the performance of the dam-foundation system, and the mechanism needs to be studied to find proper treatments in giant rock engineering. Baihetan Dam is a high arch dam with typical nonsymmetry problems, and is studied in this paper as an example. A geomechanical model test was conducted focusing on features of deformation and failure phenomena, and a numerical calculation based on a nonlinear finite element method (FEM) was performed on it. Deformation reinforcement theory was particularly involved in the FEM calculation to quantize and describe the instability status of structure and proved to be reliable. It is found that the nonsymmetrical profile causes the allocation of arch thrust to be asymmetrical, leading to an approximately equivalent rotation of asymmetric axis of deformation. This phenomenon contributes to causing local regions of the dam to be under an extra large tension or compression in the overload process. The asymmetrical geological conditions, characterized by many developed tectonic surfaces in the left abutment, are revealed to threaten the stability of the rock mass. Global safety factors of the dam decrease as a consequence, when comparing the results with other dams of similar dam height. In the end, the revised definition of Lombardi's slenderness coefficient was proposed considering nonsymmetry of the profile.

**Keywords** High arch dam · Nonsymmetry · Engineering geology · Geomechanical model test · Nonlinear finite element method · Stability assessment

## Introduction

Arch dams, especially with a height of around 300 m, have been built more during the past several decades around the world, and some are still planned to be built currently. These so-called high concrete arch dams have a greater dependence on structural stability and engineering safety from many unfavorable factors due to their higher level of stress and security requirement. No obvious topological or geological nonsymmetry problem is encountered in many dams, so that an arch structure can work as usual, and the structure can maintain a superior level of stability. However, there are some other high arch dams located in nonsymmetrical canyons or with obviously nonequivalent geological status between two side foundations. This nonsymmetry is likely to affect the working condition of a dam and should be carefully considered during periods of design and construction.

Malpasset Dam (Londe 1987) in France has a gentle left bank slope and an unfavorable combination of foliation and a downstream fault, and it ultimately experienced a rotation of the entire arch dam about its right bank extremity, which could explain the dam's failure. The Beauregard arch dam (Barla et al. 2010), located in Aosta Valley, Italy, has a poor quality of rock mass and a deep seated shear zone up to 20 m in the left abutment slope, which caused a continuous slope movement leading to a landslide hazard. These issues are correlated with the nonsymmetrical quality of rock mass or geotectonic conditions between the two side banks. Additionally, in some cases, an

✉ Ziheng Song  
song88823@aliyun.com

<sup>1</sup> State Key Laboratory of Hydrosience and Engineering, Tsinghua University, Beijing 100084, China

asymmetrical profile is inevitably designed due to the hard symmetrization of a canyon's shape. Inguri Dam in Georgia, of 271.5 m height, was constructed in an asymmetric canyon. The shape of the dam was optimized through a series of tests and calculations. Then antiseismic reinforcement and an enlarged concrete seat were set to improve the stress status and reduce the concrete volume of the dam (Bronstein et al. 1979). In China, Zhaolaihe Dam (Li 2001) and Jinping No. 1 arch dam (Zhou et al. 2006) also encountered the problem of a nonsymmetrical profile, and they were treated with a combination of various methods to overcome this unfavorable effect. Nonsymmetry is inevitable and is likely to destroy the conventional hypothesis that an arch works under an ideal symmetrical condition, so there is a lack of guidance in finding a solution. Optimization of the dam shape and design of reinforcement treatments meet great challenges in this case, while security requirements and engineering quantities should both be considered.

Appropriately deep foundation excavation, an artificial abutment, and a nonsymmetrical arch shape are commonly used specific to the geometrical nonsymmetry. Treatments of defective abutment rock mass and tectonic structures include anchoring, grouting, concrete plugging, and are often conducted to enhance the weak side foundation (Hu et al. 2010; Yang et al. 2013a, b). Although there are conventional methods acceptable to engineers that have been used in actual projects, the mechanism is not yet well understood. Current design specifications or criteria (US Bureau of Reclamation 1977; SL282-2003; DL/T 5346-2006) have not recommended specific treatment of this nonsymmetry problem.

Characterized by its strong nonsymmetry status, Baihetan arch dam in southwest China, which is planned to be built, is taken as a case study in this paper. To solve the problems, the characteristics of mechanical behavior and its failure scenarios would be investigated firstly. A geomechanical model test and FEM calculation are the most common and effective methods in this investigation. By model test, the complex real structure is reproduced on a reduced scale model, and an overloading rupture test is performed on it. The data, including displacement strain, can be acquired and the failure pattern and cracking process can be directly perceived (Fumagalli 1973; Lemos et al. 1995; Fei et al. 2010; Liu et al. 2013). The model test cannot be repeated once the model is ruptured, and it takes too much time building the geomechanical model. Three dimensional FEM calculations (Yu et al. 2005; Oliveira and Faria 2006; Zhang et al. 2008; Jin et al. 2011) can verify the result from the laboratory and supplement the result to give a more detailed mechanical illustration and analysis of the structure. Both of these

methods are used herein, mainly focusing on the effect of nonsymmetry.

Deformation reinforcement theory (Yang et al. 2008, 2013a, b) was involved in the FEM simulation to describe the mechanical states of the structure and its stability in a more persuasive way, and to help to interpret the failure phenomena observed by the model test. The result shows a good consistency with that from the experiment. A comparative study procedure (Jin et al. 2011) was used to help to emphasize the effect of nonsymmetry, by comparing the results with that of some other high arch dams in China. Finally, a modified definition of slenderness coefficient is proposed. Then, by introducing the definition of nonsymmetry ratio, dams with a close conventional slenderness coefficient, but different bearing capacity can be distinguished.

### Baihetan arch dam

Baihetan arch dam and hydropower project is located on Jinsha River in Yunnan Province, southwest China (Fig. 1). The barrage is designed as a double-curvature concrete arch dam, with a maximum height of 289 m and normal water level of el. 834 m.

The dam site is an asymmetric, V-shaped gorge, with a steeply sloping right bank and gently sloping left bank, where the right bank is almost 300 m higher than the left (Fig. 2). The distance from the centerline of the river to the left arch abutment is 100 m larger than to the right at the elevation of the dam crest, as shown in Fig. 3.

The rock mass of the dam foundation is mainly composed of hard basalt including aphanitic basalt, amygdaloidal basalt, and meta-basaltic breccia lava, the formation of which belongs to the Emeishan Group of the Upper Permian, and flow layers are inclined with strike trending  $N30^{\circ}\text{--}50^{\circ}\text{E}$  with dip angle of  $SE15^{\circ}\text{--}25^{\circ}$ . The columnar jointed rock mass is fully developed in the lower portion of left bank foundation (Jiang et al. 2014). The weathering and unloading areas in left bank are generally larger than the right bank. The horizontal depth of the strongly unloading zone in the left bank is 0–43 and 33–123 m at the slightly unloading zone, compared with that of 0–49 and 29–77 m in the right bank, respectively. The horizontal depth of the slightly weathered zone lower limit is 74–130 m in the left bank and 27–39 m in the right bank. The rock quality of the right bank abutment is generally better than that of the left bank.

Fault tectonics, disturbed belts, and interlayer belts are well-developed at the dam site; the fault tectonics and crush belts at the left bank develop better than right bank. As shown in Fig. 3, the left abutment rock masses are cut by these discontinuities, where the integrity of rock mass

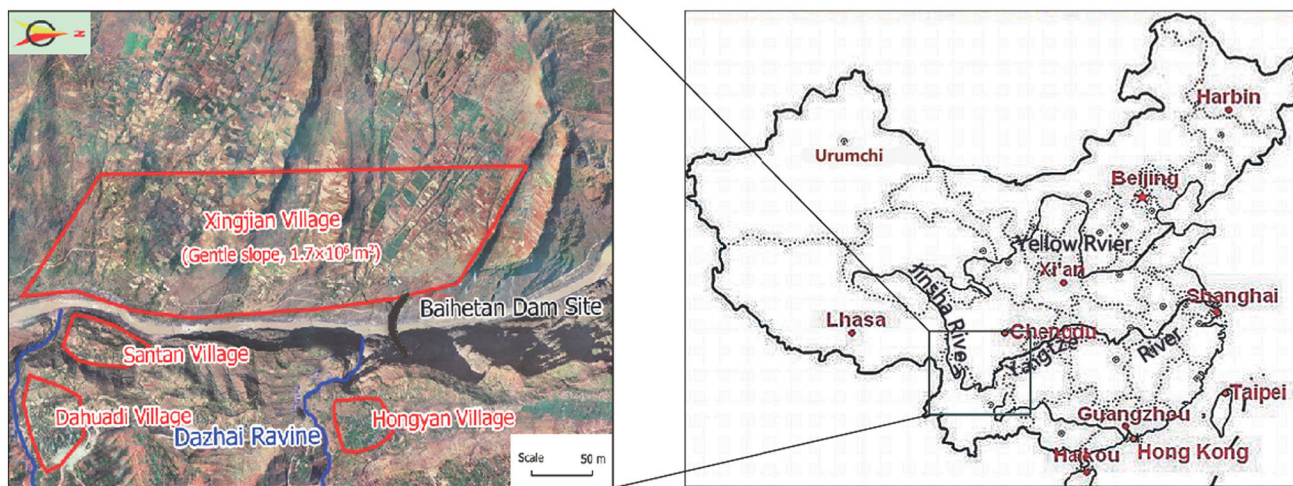


Fig. 1 Location of Baihetan arch dam in China, and a closer view of the dam site

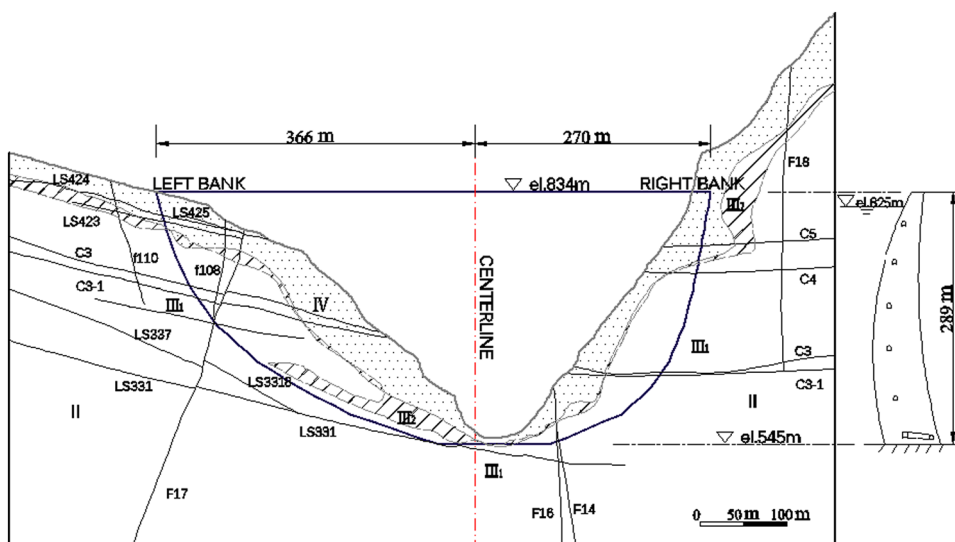


Fig. 2 Panoramic photograph of the Baihetan dam site: the slope of the left bank low and gentle, and the right bank slope is high and steep

decreases and its entire bearing capacity will be consequently influenced.

The shape of the dam is designed to be asymmetric due to aforementioned topological and geological asymmetry between both sides of the foundation. With the total 702.3 m arc length of arch at dam crest, the left part is 412.0 m long and the right part is 390.3 m, divided by a centerline. As a result, the left part of the upstream surface is larger than the right part, causing the transverse projection of the normal water load to be 267,000 N towards the right bank. If the profile is totally symmetric, the transverse projection of the upper water load would be 0. Asymmetric distribution of static water load, asymmetric profile, and nonequivalent geological conditions causes the behavior of this dam to be different from symmetric dams.

Fig. 3 Profile of Baihetan arch dam and layout of geological conditions at dam site



## Geomechanical model test

### Similarity coefficient

The relations of geometrical size and material parameters between the model and prototype are established by similarity constants (Fumagalli 1973, 1979; Liu et al. 2003; Fei et al. 2010), which are defined as the ratio of the physical quality of prototype  $q_p$  to that of the prototype  $q_m$  correspondingly:

$$C_q = \frac{q_p}{q_m}, \quad (1)$$

where the quantity  $q$  can be length, stress, strain, displacement, deformation modulus, density, Poisson's ratio, friction coefficient, shear strength, cohesion force, etc. In this paper, the geometrical similarity constant was chosen to be 250, and the similarity coefficient of unit weights was 1.0. The other similarity coefficients can be obtained by dimensional analysis, as shown in Table 1.

### Simulation methodology

To meet the requirement restricted by material similarity coefficients, the model material would have high density, low Young's modulus, and low strength. Barite powder, glue, and bentonite were mixed to be the experimental material. The mixture proportion was determined by material testing before the model was built.

Small block masonry technology (Zhou et al. 2005; Liu et al. 2013; Zhang et al. 2014) was employed in the model construction, in which pre-pressed small blocks were piled with a special cement binding them together. The vital tectonic discontinuities were simulated by dehydrated gypsum and iridescent paper. The deformation capacity and friction resistance of interfaces can be simulated by the two materials separately.

Faults F14, F16, F17, F18, f114, and f108, staggered zones C3, C3-1, C4, LS331, LS3318, and LS337, and joints J110, J139, and J101 were modeled. Among these structure surfaces, F18 and C4 are located on the right bank only, F16, C3, and C3-1 lay across the valley, and the other tectonic structural surfaces are all located on the left bank (as shown in Fig. 4). The mechanical parameters of the dam and rock masses are listed in Table 2, and parameters of the main surfaces are shown in Table 3.

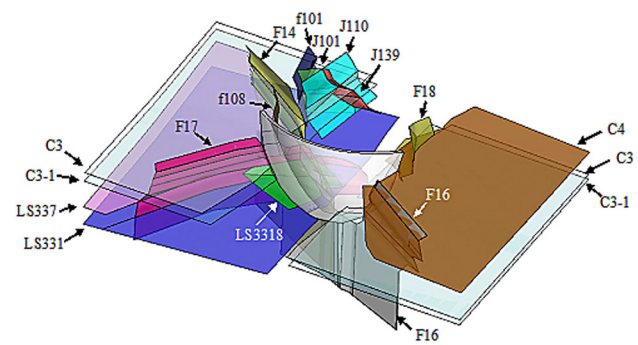


**Fig. 4** Schematic diagram of dam and discontinuities simulated

The simulated range of the prototype extends 0.6 times the dam height (185 m) upstream, 3.3 times (950 m) downstream, about 2 times (575 m) from the centerline to the left and right side, and 0.8 times (230 m) deep under the dam bottom. As the geometric similarity constant is 250, the size of the model can be obtained, where it is fixed in a 4.6 m × 4.6 m × 2.8 m sized box-shaped steel frame (Fig. 5).

Self-weight action and hydrostatic pressure acting on the upstream surface were modeled in this test. Self-weight action was simulated by the model materials using similarity of unit weight  $C_\gamma$  equals 1. Upstream hydrostatic water pressure was applied by 61 jacks arranged in eight layers on the upstream face. Jacks of the same layer were grouped by one oil separator with their respective oil pumps to provide pressure and modified by precision pressure gages controlling the pressure in layers. Step loading on the model was carried out during the overloading process. A cyclic loading procedure was performed when the structure was in elastic status with incremental load  $0.2P_0$  ( $P_0$  indicates the normal water load), and a continuous loading procedure without unloading was then performed after that until structural failure takes place.

Deformation and its development processes of each point on or inside the model are the main objectives of monitoring, captured by strain gages, internal and external displacement sensors. These monitored points were on the surface of the dam and foundation, as well as on the faults and belts faces inside the foundation. These measured data were gathered by UCAM-70A with a precision of 0.001 mm. Moreover, eight digital cameras were set up at the dam toe, heel, and arch sides to record the cracking process in these areas.

**Table 1** Similarity constants of geomechanical model

Unit weight $C_\gamma$	Length $C_L$	Strain $C_\epsilon$	Stress $C_\sigma$	Displacement $C_u$	Poisson ratio $C_\mu$	Friction angle $C_f$	Cohesion $C_c$	Elastic modulus $C_E$	Shear strength $C_\tau$
1	250	1	250	250	1	1	250	250	250

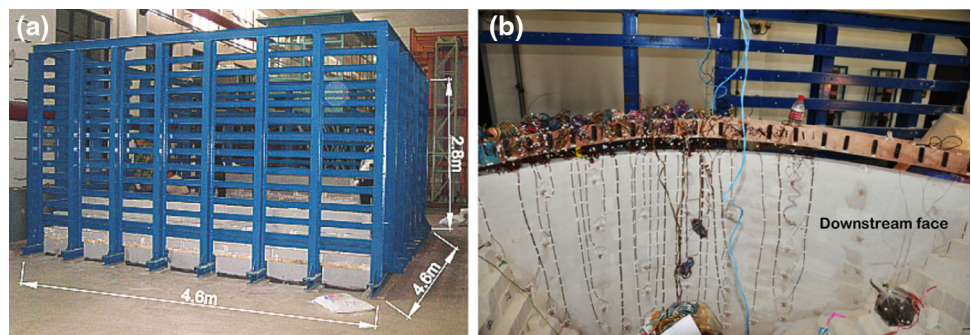
**Table 2** Mechanical properties of dam and rock masses

Material	Density (KN/m <sup>3</sup> )	Deformation modules (MPa)		Poisson's ratio	Friction angle	Cohesion (MPa)		
		Prototype (×10 <sup>4</sup> )	Model			Prototype	Model (×10 <sup>-4</sup> )	
Dam	Concrete	24	2.4	96	0.17	1.6	2.5	100
Rock mass	II	28	1.8	72	0.22–0.24	1.2–1.4	1.3–1.5	52–60
	III <sub>1</sub>	27–28	1.3	52	0.24–0.26	1.0–1.2	0.8–1.0	32–40
	III <sub>2</sub>	26	0.9	36	0.26–0.28	0.8–1.0	0.6–0.8	24–32
	IV	25	0.4	16	0.30–0.32	0.7–0.8	0.5–0.6	20–24

**Table 3** Material parameters of major discontinuities

	Thickness		Deformation modules (MPa)		Friction angle	Cohesion (MPa)	
	Prototype (m)	Model (cm)	Prototype (×10 <sup>4</sup> )	Model		Prototype	Model (×10 <sup>-4</sup> )
F14, F16	0.4	0.16	1	40	0.45	0.1	4
F17	0.6	0.24	1	40	0.35	0.05	2
F18	0.8	0.32	1	40	0.4	0.05	2
f108	0.1	0.04	1.2	48	0.43	0.08	3.2
C4	0.1	0.04	0.15	6	0.25	0.02	0.8
C3	0.2	0.08	0.25	10	0.45	0.1	4
C3-1	0.2	0.08	0.25	10	0.38	0.07	2.8
LS337	0.1	0.04	0.25	10	0.38	0.07	2.8
LS331	0.2	0.08	0.1	4	0.55	0.15	6
LS3318	0.2	0.08	0.1	4	0.38	0.07	2.8

**Fig. 5** Test system of Baihetan Dam: **a** testing frame where the geomechanical model is located, **b** close view of dam model



**FEM calculation**

**Deformation reinforcement theory (DRT)**

Concepts of action and resistance are involved in DRT to evaluate the stability of a structure in a generalized way, based on a transition from the consideration of a rigid body to that of a structure composed of elastoplastic material. When a structure is under a certain action, current stress field satisfying the equilibrium condition is regarded as equivalent to the external load, and another hypothetical

stress field satisfying the yield criterion of material anywhere then denotes the resistance capacity of the structure. In the sense of FEM, two stress fields can be expressed as (Yang et al. 2013a, b):

$$S^{eq} = \left\{ \sigma^{eq} | \mathbf{F} = \sum_{i=1}^N \int_{v_i} \mathbf{B}^T \sigma^{eq} dV \right\}, \tag{2}$$

$$S^{yc} = \{ \sigma^{yc} | f(\sigma^{yc}) \leq 0, \text{ in all } v_i, i \in \{1, 2, \dots, N\} \}, \tag{3}$$

where  $\mathbf{F}$  is the equivalent nodal force representing the external actions,  $N$  denotes the total number of elements in

the FE model,  $\mathbf{B}$  denotes the displacement gradient matrix,  $v_i$  is the volume of element. Generalized action and structural resistance are respectively represented by  $S^{\text{eq}}$  and  $S^{\text{yc}}$  on the scale of elements, and the exact  $S^{\text{yc}}$  can be specified corresponding to  $S^{\text{eq}}$  by the closet point project method (Simo et al. 1988). When these two stress fields are unable to reach consistency by calculation of conventional FEM, DRT allows them not to be satisfied simultaneously (Yang et al. 2013a, b). Then, the unbalanced force  $\Delta Q$  is proposed to describe the gap between action and resistance in the form of equivalent nodal force, and the plastic complementary energy  $\Delta E$  is defined as:

$$\Delta Q = \sum_{i=1}^N \int_{v_i} \mathbf{B}^T (\boldsymbol{\sigma}^{\text{eq}} - \boldsymbol{\sigma}^{\text{yc}}) dV \quad (4)$$

$$\Delta E = \sum_{i=1}^N \int_{v_i} \frac{1}{2} (\boldsymbol{\sigma}^{\text{eq}} - \boldsymbol{\sigma}^{\text{yc}}) : \mathbf{C} : (\boldsymbol{\sigma}^{\text{eq}} - \boldsymbol{\sigma}^{\text{yc}}) dV, \quad (5)$$

where  $\mathbf{C}$  is the elastic compliance tensor. The existence of unbalanced force suggests the location and magnitude of regional insufficiency of structural resistance. The unbalanced force takes a vector form providing a quantized method describing the unstable status of the structure, and the plastic complementary energy (PCE) integrates the gap between  $S^{\text{eq}}$  and  $S^{\text{yc}}$  in Euclid space, giving an overall evaluation of this instability in a scalar form. Based on the statistics of PCE of elements in some region, the stability is quantized, negatively relative to the value of the regional PCE. This theory has been used in stability assessment of many high arch dams and slopes (Yang et al. 2008; Liu et al. 2012) and has also been introduced into fracture analysis of brittle materials (Pan et al. 2013).

### FE model of the Baihetan arch dam

A three-dimensional FE model (Fig. 6) was developed to verify the result of the experiment and offer some other perspectives to study the interaction behavior between the dam and foundation in detail. The FE model simulates a domain with 1.5 times the dam height (528 m) upstream, 2.3 times (672 m) downstream, nearly 3 times (800 m) in the left and right bank directions, 200 m above the dam crest, and 2 times the dam height (578 m) below the dam bottom. The total size of the model is 1600 m  $\times$  1200 m  $\times$  1067 m, and the number of elements and nodes are 116,506 and 127,779 separately.

Classification of rock and tectonic structural surfaces at the dam site were simulated in the model, and the material parameters are the same as that used in the geomechanical model test. The Drucker–Prager criterion was used as the yield criterion for materials of both dam and foundation,

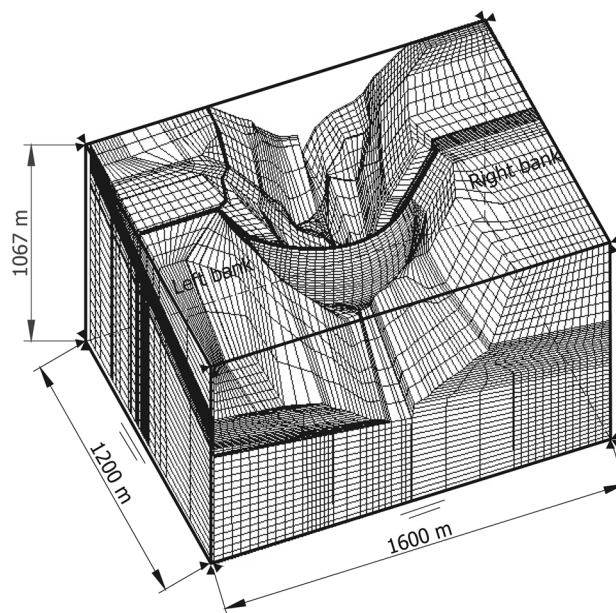


Fig. 6 FE mesh of Baihetan Dam

and an ideal elastic–plastic model was involved in the 3-D nonlinear FEM calculation, using a self-compiled program TFINE. The FE analysis was performed on a computer with Intel Core i7-3770, 3.4 GHz CPU and 16 GB of memory. To keep consistency with the load case simulated in the geomechanical test, hydraulic pressure on the downstream face and temperature load was neglected, without losing generality of the topic in this paper, as the upstream water load plays a prominent role in the overload process. The loads applied on the structure are simulated progressively in the following scheme: (1) gravity field of the massif was calculated as the initial condition previously; (2) gravity of the concrete dam was applied additively to the first step; (3) hydrostatic pressure was then applied on the upstream face as the case of normal water load; (4) 0.5 times the hydraulic pressure was set as a load step, until 4 times the water load was applied.

### Comparative cases of high arch dam

Three other double curvature high arch dams in China with similar dam height, Jingping (Zhou et al. 2006; Fei et al. 2010), Xiluodu (Liu et al. 2013; Lin et al. 2014), and Xiaowan (Jin et al. 2011; Lin et al. 2014) arch dams, are specially cited here as comparative cases. Each of them denotes a different magnitude of nonsymmetry. The comparison is based on the result from the same simulation theory or calculation method, which had been conducted for former projects. The typical geometrical parameters are listed in Table 4. Baihetan is the second lowest dam among the four dams, and its dam crest chord length is the second

**Table 4** Typical geometrical parameters of arch dams

	Baihetan	Jinping	Xiluodu	Xiaowan
Dam height (m)	289	305	278	294.5
Chord length <sup>a</sup> (m)	626.6	482.8	587.5	891.3
Arch length <sup>a</sup> (m)	702.3	552.3	679.0	800.1
Upstream area (10 <sup>4</sup> m <sup>2</sup> )	15.3	10.9	13.0	17.1
$F_x^b$ (10 <sup>4</sup> t)	-26.7	-17	-9.7	36
$F_y^b$ (10 <sup>4</sup> t)	1645	1281	1274	1724

<sup>a</sup> The chord length and arch length are measured on the dam crest

<sup>b</sup>  $F_x$  and  $F_y$  are downstream and transverse components of normal water load

longest. The nonsymmetry characteristics of Baihetan are the most apparent, and the wide canyon makes the nonsymmetry more significant to its performance. The profile shape and geological condition of the foundation make the Jinping arch dam also a relatively less nonsymmetrical dam. Xiluodu can be considered an arch dam with good symmetry and with the lowest dam height.

## Results

### Displacement analysis of the dam

Displacements of the downstream face from numerical and experimental results and comparison of relative downstream displacement with the other three dams are shown in Fig. 7. The relative displacement is obtained by displacement of the left cantilever minus that of right cantilever. The displacements from model test are converted to that of prototype, of which direction along the river is defined as positive.

The largest displacement obtained takes place on the crown cantilever at the dam crest, with the downstream component 149 mm (Fig. 7a). The numerical results show good consistency with that monitored in the test, which makes both methods reliable. Because of the larger area of the left part of the upstream face, the softer rock mass of the left bank foundation, and the cutoff of the rock mass formed by discontinuities, the deformation of the lower left part of the dam is larger than the right part. Taking displacements at el. 620 m by the model test as an example, the downstream displacement of the left cantilever (35.1 mm) is about twice as large as that of right cantilever (17.4 mm).

Curves of relative downstream displacement between the left and right cantilevers by the model test show the phenomenon caused by nonsymmetry (Fig. 7b): curves of nonsymmetrical dams including Baihetan and Jinping cross the vertical zero line. The relative displacements vary more inconsistently and intensively along the dam height,

according to the gradient and turning point of the curve at some elevations. In this sense, the dam body takes an apparent asymmetrical deformation than the symmetrical dams, and the relation of their magnitudes between the two side banks changes along the dam height.

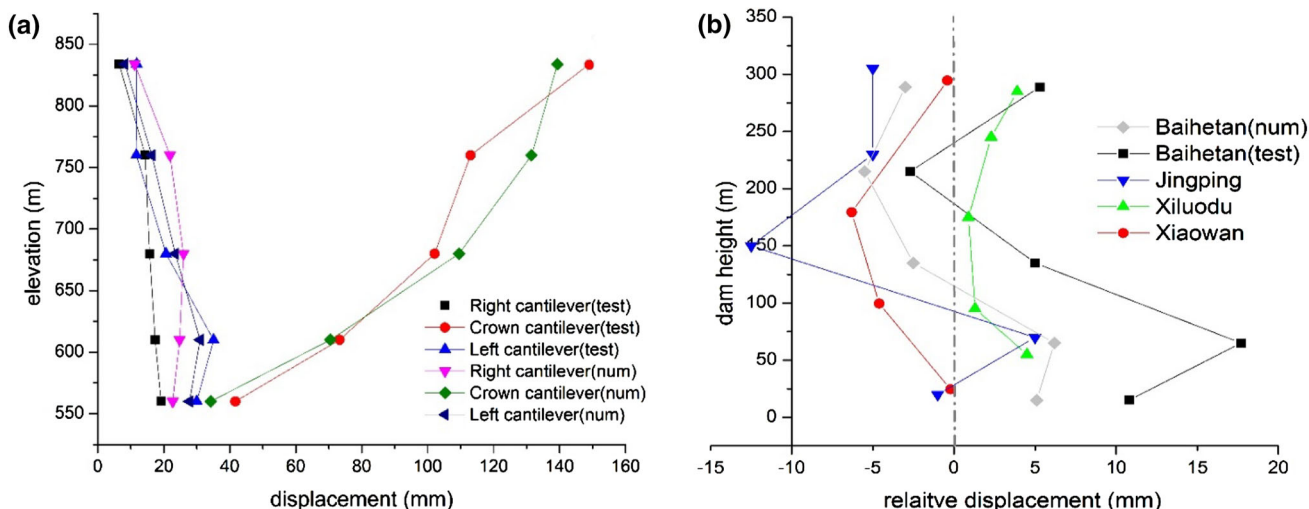
The configurations of relative deformation at two elevations, shown in Fig. 8a, are formed by setting the right abutment as a reference point. The experimental result is larger than the numerical result at some points, but with similar direction. The left arch abutment at el. 760 m trends to move upstream, while it takes the opposite direction at el. 620 m. Figure 8b shows the deformed mesh of the dam, giving a clearer view that the place of largest deformation offsets from the centerline to the left. It can be viewed as the symmetry axis of deformation offsetting with a certain degree. This offset, combined with the restriction from the rock mass under the dam base, results in a kind of distorted deformation of the dam body.

### Deformation development during overload process

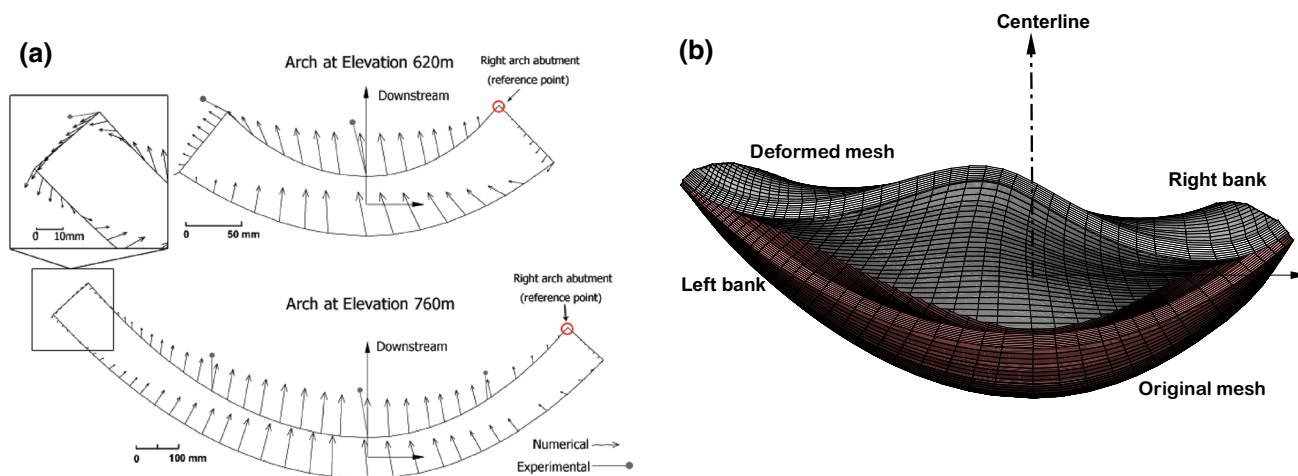
The structure stayed at an elastic stage under normal water load, and no crack occurred on the dam or foundation. When the overload process started, the displacements of each monitoring point developed with different degrees. The process of this development is represented versus the overload factor  $K$ , defined as the ratio between current water load applied on the upper surface and the normal water load.

Figure 9 shows the development processes of displacement on arch abutments at three different elevations. The downstream displacements increase regularly faster since  $K = 3.0$  (Fig. 9a), indicating plastic phase in some areas of the dam and stress redistribution. The displacement of the right arch abutment at el. 680 m decreases abruptly when  $K > 7.0$  (Fig. 9a), as a result of the dominating horizontal crack on the left part of the downstream surface, which will be discussed below. It is obvious that the downstream displacements of the left abutment are larger than that of right abutment. In addition, the rate of increment grows as the elevation decreases, and asymmetric deformation is aggravated during the overload process. This phenomenon was also observed by Fei et al. (2010) on their geomechanical model test for Jinping Dam, a clockwise rotary movement happened on the dam body during the overload process, with greater displacement of left abutment than the right, while the deformation was basically symmetric under normal conditions.

Displacements cross the river of some monitored points at arch abutments, decreasing before  $K = 2.0$  (Fig. 9b, direction towards the bank on its own side is defined as positive), which means that these points tend to move towards the riverbed. This phenomenon has a certain



**Fig. 7** Downstream displacements analysis **a** downstream displacements on downstream face, **b** relative displacements between the left and right side cantilevers



**Fig. 8** Deformation of Baihetan Dam **a** relative deformation of arches, **b** deformed mesh of the dam from the numerical result (magnified)

relation with the shape of dam and complex geological condition of the left foundation. Until  $K$  reaches a certain value, the displacement of a point on the right arch abutment at el. 680 m stops developing, where the large cracks nearby block the spread of stress in this region.

It is worth mentioning that downstream displacement on the left abutment at el. 572 m increases fastest, and transverse displacement at el. 572 m increases slowest. Arch action is weaker and cantilever action is stronger at lower elevation during the overload process, and it is more obvious in the left part relatively.

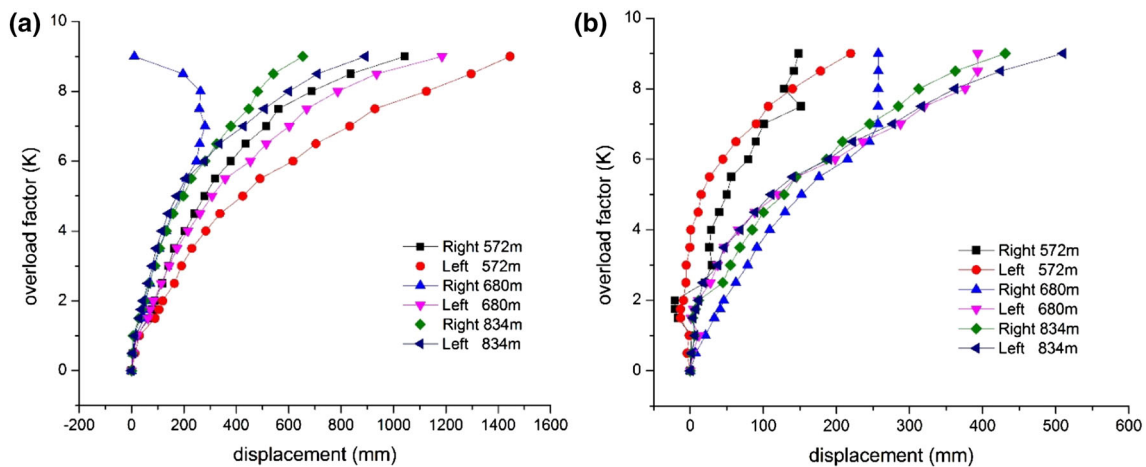
**Stress analysis of the dam**

Figure 10 represents the stress distribution on dam surfaces under normal water load obtained by laboratory test, in the

vector graphic form. The maximum tensile stress was observed in the left dam heel area on the riverbed (2.31 MPa), and the maximum compressive stress on the upstream face appeared on the crown cantilever at el. 696 m (4.03 MPa). There is no tensile stress observed above el. 620 m. The maximum compressive stress on the downstream face was on the little left portion of the dam toe (9.82 MPa), and some third principal tensile stresses were observed on the downstream surface on the left arch abutment at el. 760 m and el. 610 m.

By statistical analysis of the element stresses for the arch abutment, the resultant force acting on each side of the arch abutment can be obtained. This describes how hydraulic pressure is generally allocated on the dam base. As shown in Fig. 11, the downstream component of arch thrust distributes mainly owing to the area difference of the left and





**Fig. 9** Development of arch abutment displacements during the overload process **a** displacements along the river (downstream is positive), **b** displacements across the river (pointing to each side bank is positive)

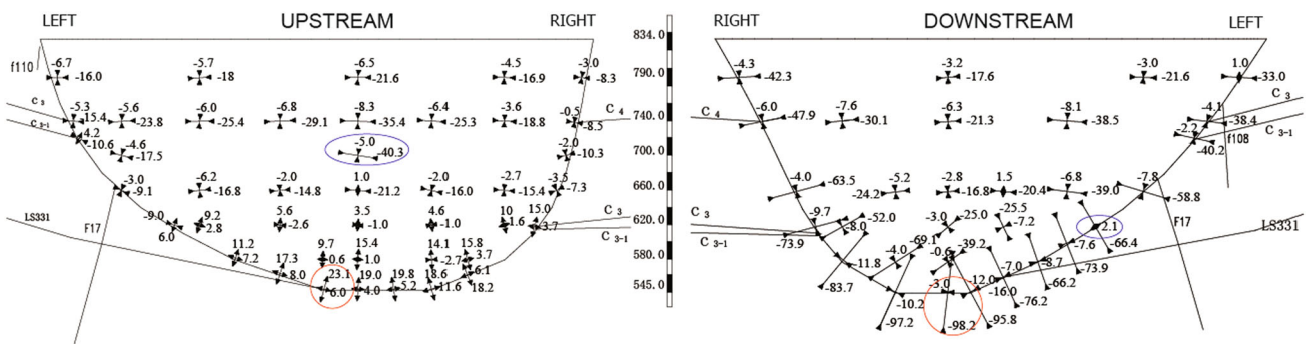


**Fig. 10** Distribution of measured stresses on dam surfaces by model test (including the first and the third principle stresses at each point, unit: 0.1 Mpa)

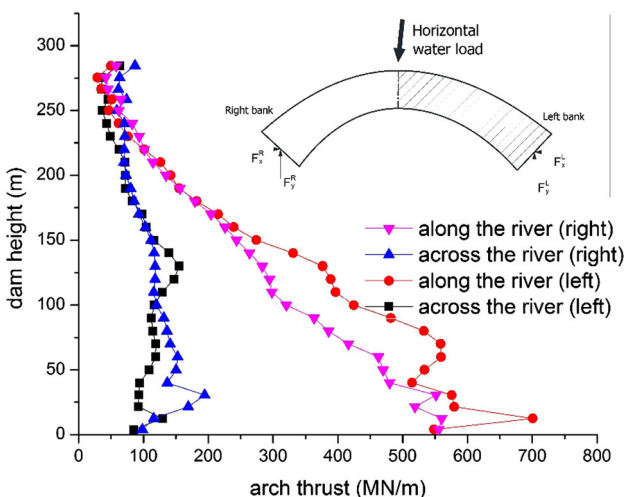


**Fig. 11** Distribution of arch thrust on the arch abutments along the dam height

right face of the dam. The thrust of the left abutment is larger than the right side below el. 700 m. Distorted distribution of thrust is emerged in the transverse components,

where the relation of their magnitudes between the two sides changes along the dam height. From a more general perspective, statistics were conducted for three-portion division (Fig. 12), and horizontal angles between the resultant thrust and transverse direction of the river are listed. The relation of the transverse components of thrust on the two sides changes between neighbor portions in the three parts. The downstream component of thrust on the left arch abutment stays larger than the right side in the middle and lower portions. The horizontal angle of the left arch abutment stays smaller than that of the right side, which is adverse to the stability of the left abutment rock (Fig. 12).

### Cracking process of dam and abutment

The videos recorded by a digital video system, analysis of measured displacement and strain, and direct observation of the model help to trace the cracking process on dam faces, abutment, and slope. During the stage of normal load, no crack was observed. When  $K = 1.3\text{--}1.5$ , a

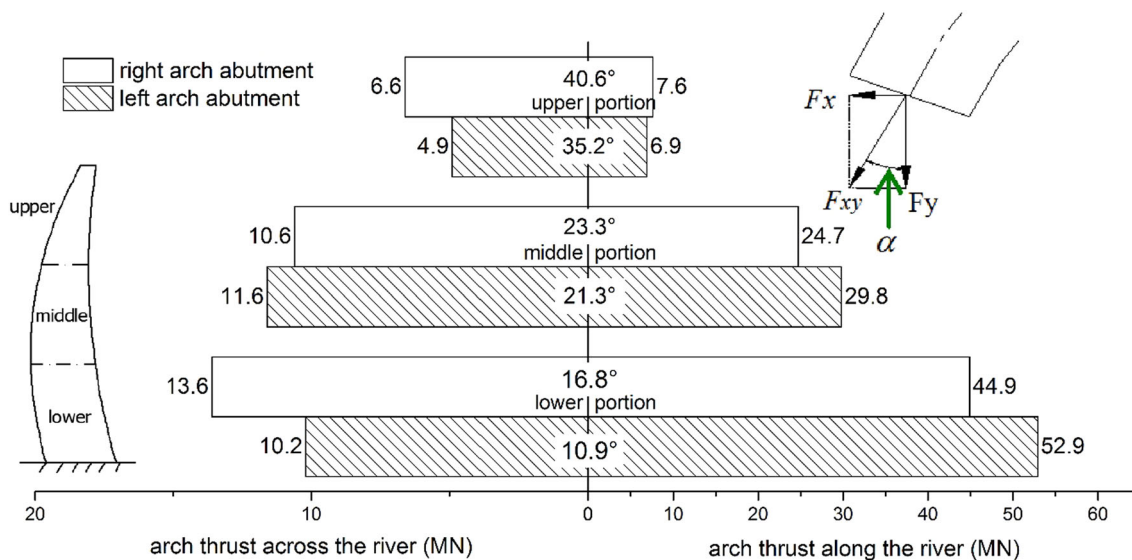


**Fig. 12** Statistics of arch thrust divided by three parts and horizontal angles of the resultant force

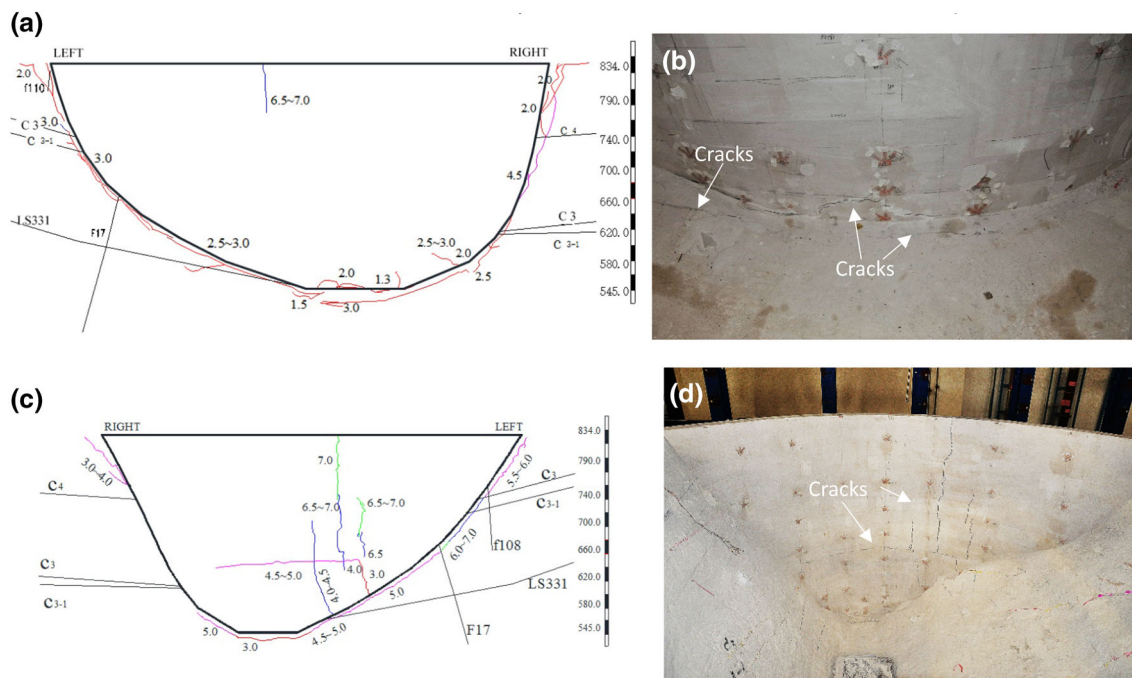


**Fig. 13** Schematic diagram and photograph of cracks on dam surfaces. **a** Schematic cracking process of upstream face, **b** photograph of cracks on partial upstream face, **c** schematic cracking process of downstream face, **d** photograph of cracks on downstream face

horizontal tensile crack initiated on the bottom of the left dam heel, and then another one occurred on the right dam heel, but neither of them extended obviously after that (Fig. 13a). When  $K$  reached 2.0, the abutment near the crest of both sides of the upstream face began to fracture, and slight cracks were observed on the middle dam heel and right arch abutment near el. 570 m. Most cracks occurred and propagated during the period when

$K = 2.5\text{--}4.0$  on the upstream abutment, from the riverbed to the outcrops of C3. Meanwhile, as shown in Fig. 13c, a crack on the downstream face started in the bottom of the dam toe and, remarkably, the left arch abutment near el. 640 m. This crack propagated regularly upward until  $K$  was 4.0, and then developed horizontally across over half of the arch until  $K = 5.0$ . At the same time, the crack of the upstream surface and foundation around it stopped

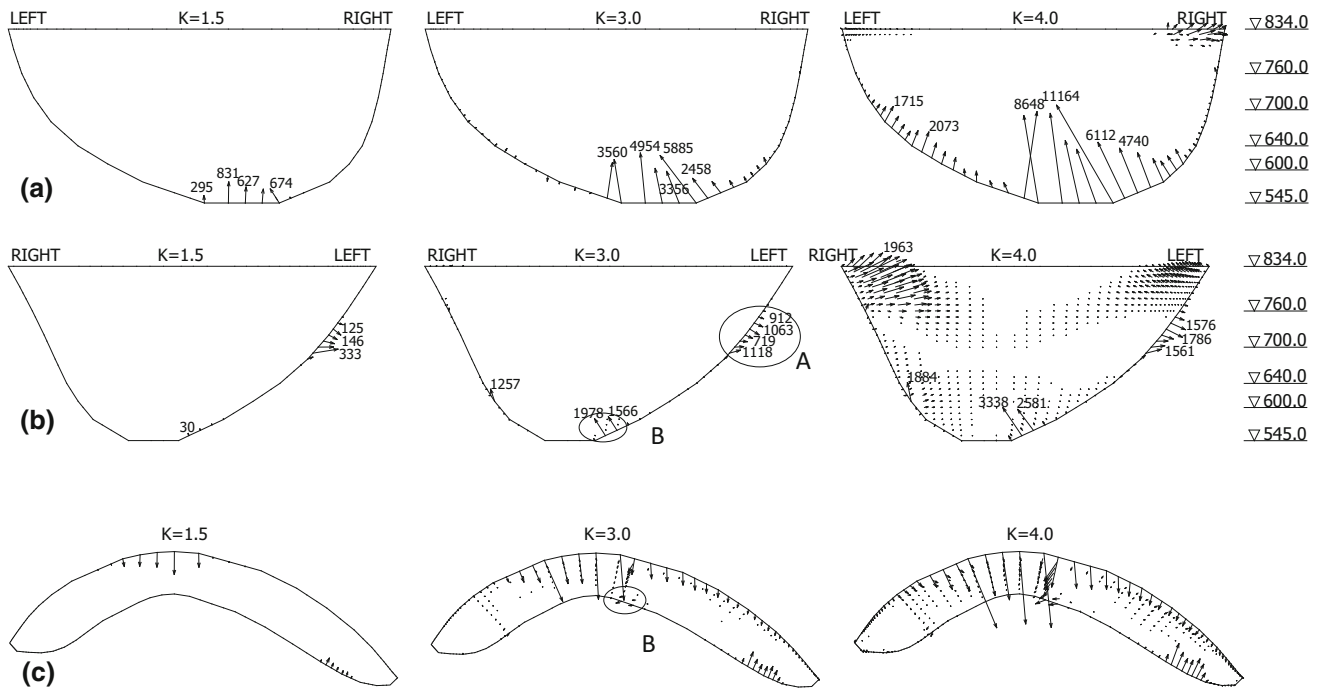


**Fig. 14** Development of unbalanced forces when  $K = 1.5, 3.0,$  and  $4.0$  **a** upstream surface, **b** downstream surface, **c** dam base surface (unit: t)

extending and no significant fracture appeared. Two vertical, long cracks branched out from the previous horizontal crack across the downstream face when  $K = 4.0-7.0$ , which caused the dam to lose its bearing capacity ultimately at the stage  $K = 7.0-7.5$ , accompanied by a connected fracture forming on the foundation surface along the entire left part of the dam toe.

The unbalanced forces, calculated by FEM, on the dam heel indicate that this area is dragged by the force from the upper left part of the dam depending on the directions (appearing when  $K = 1.5$ , Fig. 14a). These unbalanced forces increase rapidly, representing action beyond the bearing capacity of material, inducing the appearance of cracks on the dam heel, as shown in Fig. 14a. The downstream surface, under compression, turns out to be with two main areas of unbalanced forces concentrated along the left dam toe (Fig. 14b), area A and area B, where the forces take different directions. Combined with the situation on the dam base surface (Fig. 14c), it can be found that area B tends to be over-compressed when  $K = 3.0$ , with a downstream component of unbalanced force, close to the initial crack on the downstream face in the laboratory test (Fig. 14c). This result of unbalanced force under the guidance of DRT, shows good agreement with the cracking process from geomechanical test. Nonsymmetry profile caused the load action and arch action to lose its symmetry, resulting in a shift of the original symcenter to the left, where the stress is more likely to concentrate at the symcenter. Then, the unbalanced forces appear early, and the

distribution and magnitude of the unbalanced force become asymmetrical. In this study, the unbalanced force on the dam heel tends to the left bank overall, with obvious increment during overload process. On the other hand, the left dam toe suffers more compression as in area A and area B.

The nonsymmetry problems characterized by the dam shape and weakness and poor integrity of the rock mass in the left abutment, result in asymmetrical deformation of the dam when it is under normal working condition. During the overload process, this nonsymmetry is amplified, followed by the initialization and propagation of cracks. By the analysis of unbalanced forces, the region with higher risk of instability can be demonstrated in a numerical way.

**Deformation of structural surfaces and final failure mode of abutments**

According to the monitored displacements and direct observation of cracks on the slope surface, location of a potential slope collapse can be found. Through the analysis of the result, no significant fault dislocation had been observed except for the following mentioned regions.

The deformation process of serial points located on the left downstream slope close to the dam toe, near the outcrop of C3 and C3-1, respectively, are represented in Fig. 15 (direction downstream and towards the left bank are defined as positive, respectively). This suggests two different progressive movement trends of the two blocks

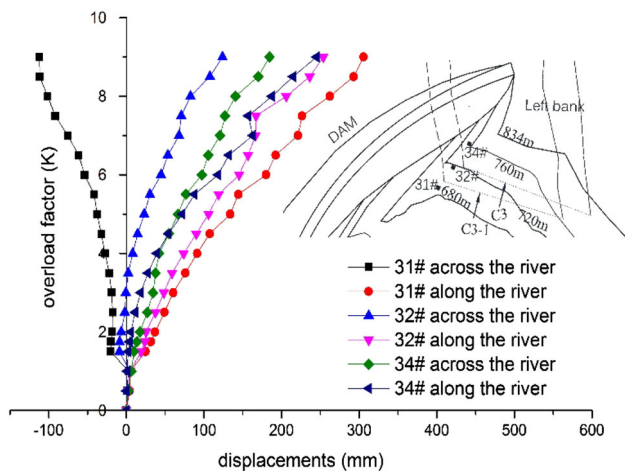


**Fig. 15** Deformation process of monitored points on the left bank slope

divided by C3-1. If surface of C3-1 was assumed to be the sliding surface, point #31 on the basal portion moved toward the river gradually during the process, while point #32 on the upper portion moved towards the left bank when  $K > 2.0$ , and point #34 above the outcrop of C3-1 moved towards the bank and downstream. The basal portion block below C3-1, specified on this slope surface area, was extruded by the upper massif with a downslope and downstream component motion relatively. In this case, two long downstream evident cracks occurred between el. 680 m and el. 720 m correspondingly (Fig. 16), since  $K$  reached 4.0.

Final failure model at different evaluation in the foundation was exhibited when the model was dismantled layer by layer, after the rupture test. The lower and upper portions in the abutment show different failure patterns, as show in Fig. 17. Between the dam base and discontinuity formed by LS3318 in the left abutment at el. 620 m, there were several parallel cracks in the arch direction, which indicates that the thrust spread from the arch causes the rock mass in this area to be under drastic compression and shear action. Cracks in both left and right abutments at el. 720 m were almost in the direction along the river or across the river.

Distributions of unbalanced forces on LS331, LS3318, and C3-1, when  $K = 4.0$ , are illustrated in Fig. 18. The unbalanced forces on LS3318 are much larger than that on LS331, with the normal direction of surface towards the dam, which means that LS3318 plays a more important role in influencing mechanical behavior of abutment rock mass, by cutting the abutment and causing the segment near the arch to be under large compressive unbalanced forces. The unbalanced forces on C3-1 also show

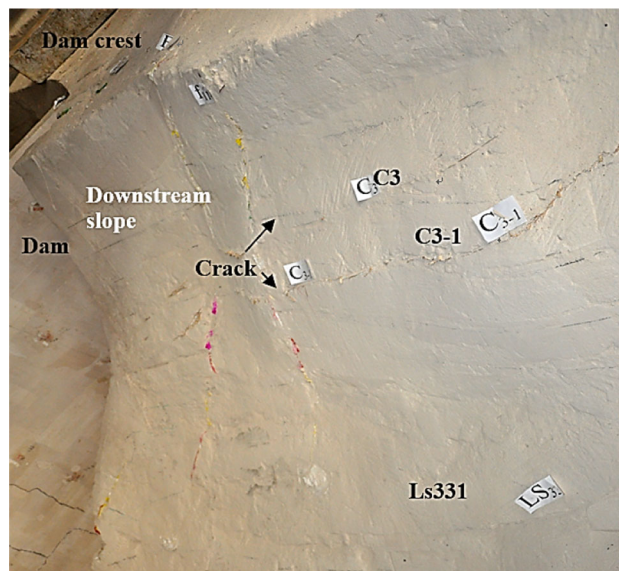


**Fig. 16** Cracks on the surface of left bank slope

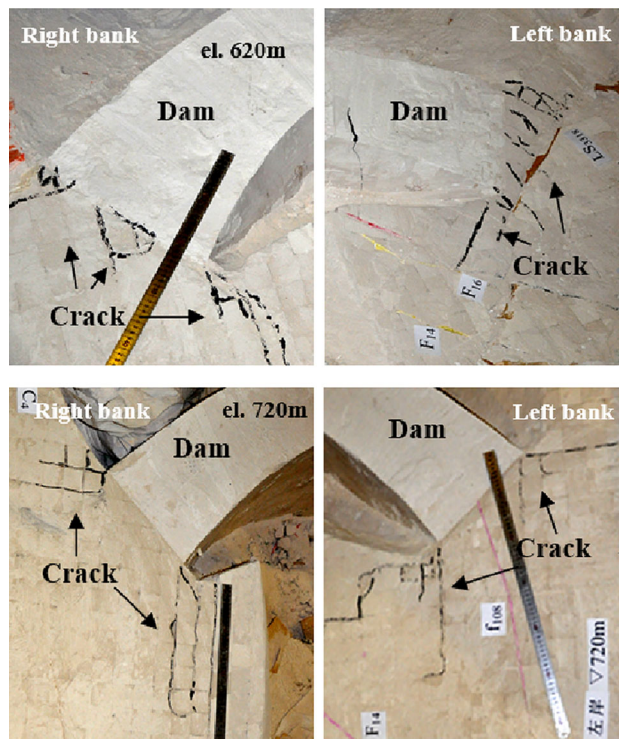


**Fig. 17** Final failure mode of abutment. **a** cracks at el. 620 m, **b** cracks at el. 720 m

agreement with the cracks observed in the test, where the forces near the outcrop drive the upper and lower portion deform as discussed before. The unbalanced force on C3-1 is smaller than that of LS3318, but its location and shear action makes the sliding collapse possible to happen.

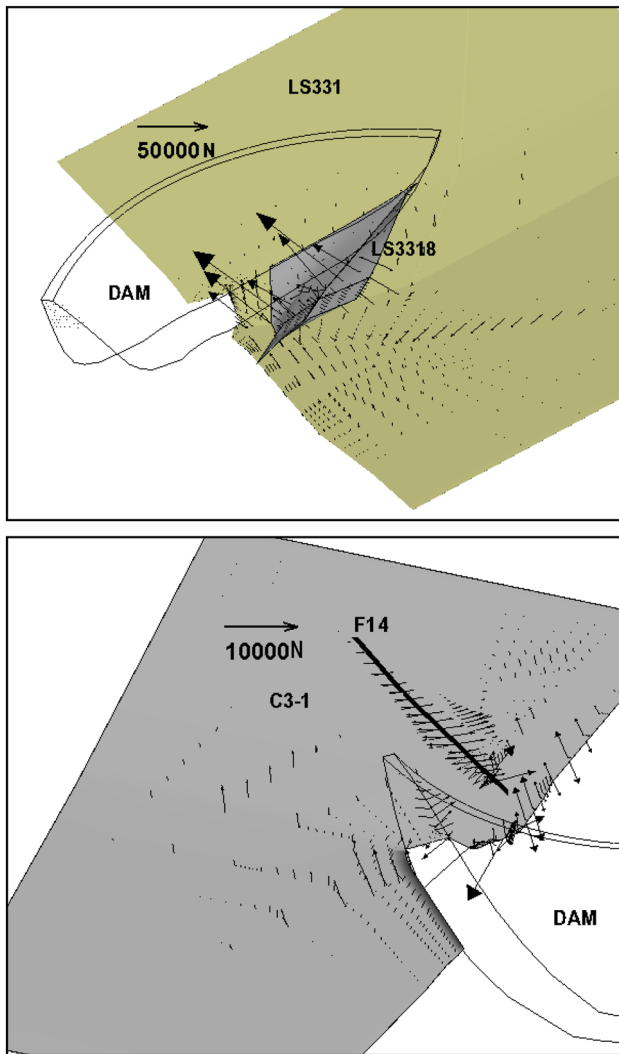


**Fig. 18** Distribution of unbalanced forces on structural surfaces when  $K = 4.0$

**Global stability analysis**

Three characteristic overload factors ( $K_1$ ,  $K_2$ , and  $K_3$ ) are conventionally extracted to denote the three main symbolic stages of structural performance during the overload process (Zhou et al. 2005; Zhou 2010; Jin et al. 2011; Cheng et al. 2014). The degree of stability is higher when the three factors are larger. Zhou (2010) defined these three factors as:  $K_1$  represents the overload factor when the crack starts,  $K_2$  represents the factor when deformation of the dam exhibits non-linear behavior and a considerable part of the dam yields, and  $K_3$  denotes the factor after which no more load can be applied on the dam as the integrity of the arch structure is destroyed. Jin et al. (2011) defined the three factors briefly summarized as the curtain safety factor, structure mutation factor, and ultimate safety factor. The definition by Zhou (2010) is adopted herein.

The three factors of Baihetan Dam obtained from mechanical test are illustrated in Table 5. Comparable results of some other arch dams, conducted by the author’s research group under the guidance of the same test methodology are also listed. The stability of Baihetan arch dam stay at a rather low level among the seven dams, with  $K_1 = 1.3-1.5$ ,  $K_2 = 3.0$ , and  $K_3 = 7.0-7.5$ . The lowest value of  $K_1$  indicates the stress status of dam is undesirable, indeed,  $K_2$  and  $K_3$  stay low as a consequence.

Statistics of PCE by regions divided into left abutment, right abutment, and dam body are made, as shown in Fig. 19. It is clear that PCE of the left abutment is larger than the right abutment, and the difference between the two sides is enlarged as  $K$  increases. This nonequivalent is remarkable as the difference is much smaller in most other dams. The difference between the two side banks indicates that the PCE of the left bank becomes the major component of the PCE of overall foundation. It is demonstrated that stability of the left bank foundation is much more significant to the global stability, which is the direct effect of the nonsymmetrical condition of geology. The key regions mentioned in section “Deformation of structural surfaces and final failure mode of abutments” are just the sources of instability that need to be reinforced.

**Discussion of slenderness coefficient considering nonsymmetry of profile**

The slenderness coefficient  $C$  of the arch dam is proposed by Lombardi (1991) as a quantity reflecting the overall geometrical characteristic in the sense of the ratio between average arch length  $L_{av}$  and average thickness  $T_{av}$ , given by

$$C = F^2 / (VH) = L_{av} / T_{av} \tag{6}$$

$$L_{av} = F / H$$

$$T_{av} = V / F$$

where  $F$  represents the area of upstream face,  $H$  is the dam height, and  $V$  is the volume of the dam. The slenderness coefficients of some arch dams are shown in Fig. 20. This coefficient is commonly accepted as an empirical method, used in shape optimization, preliminary safety assessment of the dam, and failure analysis. The evaluation based on the coefficient is always restricted by a limit line, believing that it is not reliable once the coefficient is beyond the line. It is apparent that nonsymmetry of the profile and its influence cannot be reflected by this definition.

According to the current definition, Baihetan Dam gets a smaller slenderness coefficient than symmetrical dams such as Xiluodu Dam and Ertan Dam, but exhibits a lower level of structural stability in geomechanical tests, as shown in Table 5. Moreover, nonsymmetry of the profile

**Table 5** Safety factors of different high arch dams by geomechanical test

Name	Height (m)	Slenderness coefficient	Nonsymmetry ratio	$K_1$	$K_2$	$K_3$
Dagangshan	210	11.7	–	2.0–2.5	5.5	11.0
Ertan	245	13.3	–	2.0	4.0	11.0–12.0
Laxiwa	250	10.0	–	2.0	3.5–4	7.0–8.0
Xiluodu	285	11.7	1.00	2.0–2.5	5.0–6.0	9.0–9.5
Baihetan	289	10.4	1.25	1.3–1.5	3.0	7.0–7.5
Xiaowan	292	13.4	1.04	1.5–2.0	3.0	7.0
Jingping	305	12.1	1.01	2.0	4.0–5.0	6.0–7.0

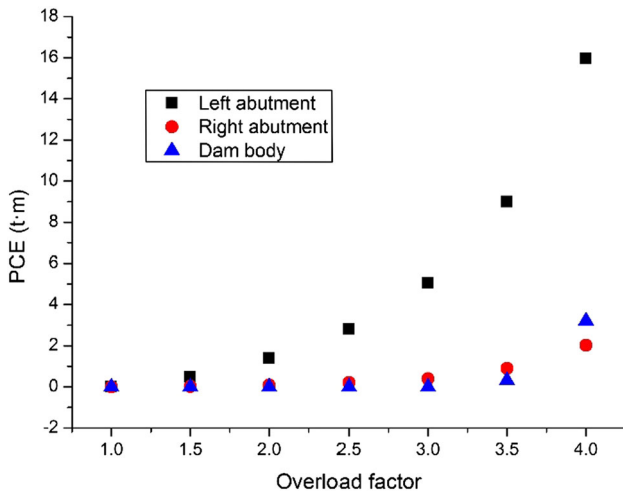


**Fig. 19** PCEs of abutment and dam body versus overload factor

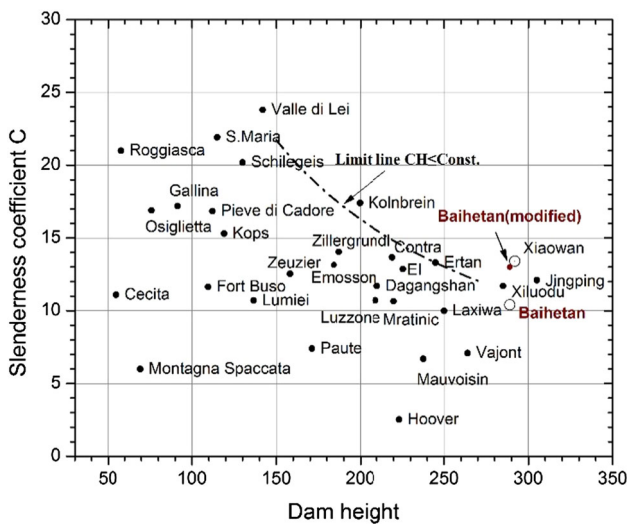


**Fig. 20** Slenderness coefficient of arch dams

can also be described geometrically, as well as the definition of slenderness coefficient. In this sense, we introduce nonsymmetry into the definition of the coefficient, by an asymmetry coefficient  $r_{as}$  (Eq. 8, calculated in Table 5). The slenderness coefficient is revised in the form:

$$C = r_{as}^n F^2 / (VH) \tag{7}$$

$$r_{as} = S_l / S_s, \tag{8}$$

where  $S_l$  is the larger area of the left or right parts of the upstream surface, and  $S_s$  implies the smaller one,  $n$  is a structural dimensionless parameter controlling the magnitude how nonsymmetry reacts to the slenderness coefficient. The asymmetry coefficients  $r_{as}$  that we can obtain are listed in Table 5.

Based on this modified definition, assuming  $n = 1$ , the slenderness coefficient of Baihetan arch dam changes to 13.0, which is a little smaller than that of Xiaowan arch dam 13.4 (Fig. 20), compared with 10.4 before the modification, near the point of Xiaowan Dam in the map. From the perspective of global stability marked by  $K_1$ ,  $K_2$ , and  $K_3$ , Baihetan arch dam studied in this paper also shows a similar level of stability as Xiaowan Dam. The revision proposed here is a proposal and needs to be investigated on many other arch dam projects. Although the nonsymmetrical profile is simply considered by  $r_{as}$  and we just check it on Baihetan Dam based on our study, the revision of the slenderness coefficient is necessary and can give a more accurate assessment of dam safety, avoiding ignorance of nonsymmetry.

### Conclusion

Baihetan high arch dam is taken as a typical high arch dam with nonsymmetry problems in a combination of topography and geology. Geomechanical model test and nonlinear FEM calculation based on DRT have been conducted to study the characteristic of structural performance. The findings and phenomena worth mention are concluded as follow:

1. A nonsymmetrical deformation along the dam height characterizes the structural behavior. The symmetry axis of deformation offset from centerline to the left bank. The lower part of the left arch abutment suffers from a more downstream component of arch thrust and less transverse component compared with that on the

right arch abutment. During the overload process, these nonsymmetrical phenomena are amplified.

2. The behavior and bearing capacity of the dam are mainly affected by cracks near the riverbed and a horizontal crack starting in the left dam toe, which has great dependence on nonsymmetry. The result of unbalanced force shows agreement with this conclusion. It is revealed that the right dam heel suffers from more tension and the left dam toe suffers from drastic compression, which decreases the stability of the dam.
3. Two key regions with potential risk are indicated both by model test and numerical calculation: The lower portion of the foundation where LS3318 cuts the rock mass nearby the dam base suffers a great arch thrust spreading from the dam and is likely to be compressed to fracture. The outcrop area of C3-1 at the left bank shows the possibility of slope collapse, with the basal portion compressed outwards.
4. By introduction of a profile asymmetry ratio, nonsymmetry is embodied in the definition of the slenderness coefficient. The modified coefficient gives a more accurate assessment of dam safety, which is more consistent with the experimental results by comparing with that of other dams.

On the basis of our analysis so far, the stability of the strongly nonsymmetrical Baihetan high arch dam is evaluated carefully. This helps to suggest a proper way to reinforce or modify the design. Meanwhile, the DRT involved in the FEM analysis has been proved to be a reliable method to evaluate the stability of the dam and abutment.

**Acknowledgments** The work reported here was supported by the National Natural Science Foundation of China under Project Nos. 51479097, 51279086 and State Key Laboratory of Hydroscience and Engineering with Grant No. 2013-KY-2.

## References

- Barla G, Antolini F, Barla M, Mensi E et al (2010) Monitoring of the Bearegard landslide (Aosta Valley, Italy) using advanced and conventional techniques. *Eng Geol* 116(3):218–235
- Bronshtein VI, Lomov IE, Menabde AY et al (1979) Arch dam of the Inguri hydroelectric station. *Hydrotech Constr* 13(12):1162–1173
- Cheng L, Liu YR, Pan YW, Yang Q et al (2014) Criterion of global stability of high arch dam structures based on model test and deformation reinforcement theory [J]. *Chin J Rock Mech Eng* 33(11):2224–2235 (in Chinese)
- Design Specification for Concrete Arch Dam DL/T 5346-2006 (2006) China Electric Power Press, Beijing
- Design Specification for Concrete Arch Dams SL282-2003 (2003) China Water Resource Press, Beijing
- Fei WP, Zhang L, Zhang R (2010) Experimental study on a geomechanical model of a high arch dam. *Int J Rock Mech Min* 47(2):299–306
- Fumagalli E (1973) *Statical and geomechanical models*. Springer, New York
- Fumagalli E (1979) *Geomechanical models of dam foundation*. Paper presented at the ISRM, Bergamo, Italy
- Hu ZX, Zhang JH, Zhou Z, Rao HL (2010) Analysis on stress and deformation of Jinping I high arch dam after foundation reinforcement [J]. *Rock Soil Mech* 09(31):2861–2868 (in Chinese)
- Jiang Q, Feng XT, Hatzor YH et al (2014) Mechanical anisotropy of columnar jointed basalts: an example from the Baihetan hydropower station, China [J]. *Eng Geol* 175(2014):35–45
- Jin F, Hu W, Pan JW, Yang J et al (2011) Comparative study procedure for the safety evaluation of high arch dams. *Comput Geotech* 38(3):306–317
- Lemos JV, Pina CAB, Costa CP et al. (1995) Experimental study of an arch dam on a jointed foundation. In: *Proceedings 8th ISRM congress, Tokyo*, pp 1263–1266
- Li HT (2001) Optimizing design of concrete double-curved arch dam of Zhaolahe hydropower station. *Hubei Water Power* 43(3):4–6 (in Chinese)
- Lin P, Zhou WY, Liu HY (2014) Experimental study on cracking, reinforcement, and overall stability of the Xiaowan super-high arch dam. *Rock Mech Rock Eng*. doi:10.1007/s00603-014-0593-x
- Liu J, Feng XT, Ding XL et al (2003) Stability assessment of the Three-Gorges Dam foundation, China, using physical and numerical modeling—Part I: physical model tests. *Int J Rock Mech Min* 40(5):609–631
- Liu YR, Wang CQ, Yang Q (2012) Stability analysis of soil slope based on deformation reinforcement theory. *Finite Elem Anal Des* 58:10–19
- Liu YR, Guan FH, Yang Q et al (2013) Geomechanical model test for stability analysis of high arch dam based on small blocks masonry technique. *Int J Rock Mech Min* 61:231–243
- Lombardi G (1991) Kolnbrein dam: an unusual solution for an unusual problem. *Int Water Power Dam Constr* 43(6):31–34
- Londe P (1987) The Malpasset dam failure. *Eng Geol* 24(1):295–329
- Oliveira S, Faria R (2006) Numerical simulation of collapse scenarios in reduced scale tests of arch dams. *Eng Struct* 28(10):1430–1439
- Pan YW, Liu YR, Cui ZX et al (2013) Fracture analysis of brittle materials based on nonlinear fem and application in arch dam with fractures. *J Appl Math* 2013:1–12
- Simo JC, Kennedy JG, Govindjee S (1988) Non-smooth multisurface plasticity and viscoplasticity. Loading/unloading conditions and numerical algorithms. *Int J Numer Meth Eng* 26(10):2161–2185
- US Bureau of Reclamation (1977) *Design of Arch Dams: design manual for concrete arch dams*. US Government Printing Office, Washington
- Yang Q, Liu YR, Chen YR, Zhou WY (2008) Deformation reinforcement theory and its application to high arch dams. *Sci China Technol Sci* 51(2):32–47
- Yang GX, Chen JY, Zhang L et al (2013a) Analysis on effect of concrete transmission and shear resistance structure in arch dam abutment reinforcement. *J Sichuan Univ (Eng Sci Ed)* 3(45):34–39 (in Chinese)
- Yang Q, Leng KD, Chang Q et al (2013b) Failure mechanism and control of geotechnical structures Constitutive Modeling of Geomaterials. Springer, Berlin, pp 63–87
- Yu X, Zhou YF, Peng SZ (2005) Stability analyses of dam abutments by 3D elasto-plastic finite-element method: a case study of Houhe gravity-arch dam in China. *Int J Rock Mech Min* 42(3):415–430
- Zhang GX, Liu Y, Zhou QJ (2008) Study on real working performance and overload safety factor of high arch dam. *Sci China Technol Sci* 51(2):48–59

- Zhang L, Liu YR, Yang Q (2014) Evaluation of reinforcement and analysis of stability of a high-arch dam based on geomechanical model testing [J]. *Rock Mech Rock Eng* 48(2):803–818
- Zhou WY (2010) Structure stability of rock mass engineering. *Chin J Rock Mech Eng* 9(29):1729–1753 **(in Chinese)**
- Zhou WY, Yang R, Liu Y et al (2005) Research on geomechanical model of rupture tests of arch dams for their stability. *J. Hydroelectr Eng* 24(1):53–58 **(in Chinese)**
- Zhou WY, Wang RK, Lin P (2006) Study on influences of asymmetry on arch dam foundation [J]. *Chin J Rock Mech Eng* 6(25):1080–1085 **(in Chinese)**